Closed-Loop Error-Correction Learning Accelerates Experimental Discovery of Thermoelectric Materials

Hitarth Choubisa, Md Azimul Haque, Tong Zhu, Lewei Zeng, Maral Vafaie, Derya Baran,* and Edward H. Sargent*

The exploration of thermoelectric materials is challenging considering the large materials space, combined with added exponential degrees of freedom coming from doping and the diversity of synthetic pathways. Here, historical data is incorporated, and is updated using experimental feedback by employing error-correction learning (ECL). This is achieved by learning from prior datasets and then adapting the model to differences in synthesis and characterization that are otherwise difficult to parameterize. This strategy is thus applied to discovering thermoelectric materials, where synthesis is prioritized at temperatures <300 °C. A previously unexplored chemical family of thermoelectric materials, PbSe:SnSb, is documented, finding that the best candidate in this chemical family, 2 wt% SnSb doped PbSe, exhibits a power factor more than 2× that of PbSe. The investigations herein reveal that a closed-loop experimentation strategy reduces the required number of experiments to find an optimized material by a factor as high as 3× compared to high-throughput searches powered by state-of-the-art machine-learning (ML) models. It is also observed that this improvement is dependent on the accuracy of the ML model in a manner that exhibits diminishing returns: once a certain accuracy is reached, factors that are instead associated with experimental pathways begin to dominate trends.

1. Introduction

Thermoelectric materials convert thermal energy to electricity based as described using the Seebeck effect, wherein a thermal gradient leads to the generation of electric current.[1] Their capacity to convert waste heat to electricity provides a route to recover the energy lost in mechanical and electrical processes.[2] Today's best-performing thermoelectric materials are particularly effective at high temperatures; and thus further progress is necessary to enable energy harvesting in low-temperature consumer applications such as IoT devices and wearables.[3,4] The design and discovery of thermoelectric materials is challenging in view of the large chemical space,[5,6] nonconvex composition–property mapping[7] and nonlinear effects of dopants on material properties.[8,9]

Large-scale chemical space searches for materials with desired properties have been pursued using high-throughput density functional theory (DFT) based simulations[10–17] and machine learning (ML) based property prediction searches.[8,18–21] Many of these studies rely on high-throughput DFT screening to rank material candidates; after which the most promising candidates are then tested in the lab.[22–24] However, the large computational cost associated with DFT calculations prohibits extensive exploration of the chemical space; and this approach does not account for the gap between simulations and experiments. The former drawback has been addressed in recent years with the help of machine learning models that learn from existing datasets and screen much larger chemical spaces.[25–27] The inability to bridge the gap between theory and experiments has been addressed in a small number of studies; valuable precedents in literature achieve this using closed-loop strategies.[28–34]

Prior such studies either required predefined functional forms for the data fusion methods to integrate available data and acquired data; or the presence of relevant sampled data to estimate the property distribution. The first requirement limits how information can be transferred between the two data sources; while the latter is computationally expensive[28] or may even be impossible to curate from available datasets. Consequently, accurate learning of material–property relationships is limited, and this militates against efficient materials exploration quantified by accuracy scores on data acquired and ranked according to performance.

H. Choubisa, T. Zhu, L. Zeng, M. Vafaie, E. H. Sargent
Department of Electrical and Computer Engineering University of Toronto
Toronto, Ontario M5S 3G8, Canada
E-mail: ted.sargent@utoronto.ca
M. A. Haque, D. Baran
King Abdullah University of Science and Technology (KAUST)
Physical Science and Engineering Division
KAUST Solar Center (KSC)
Thuwal 23955, Saudi Arabia
E-mail: derya.baran@kaust.edu.sa
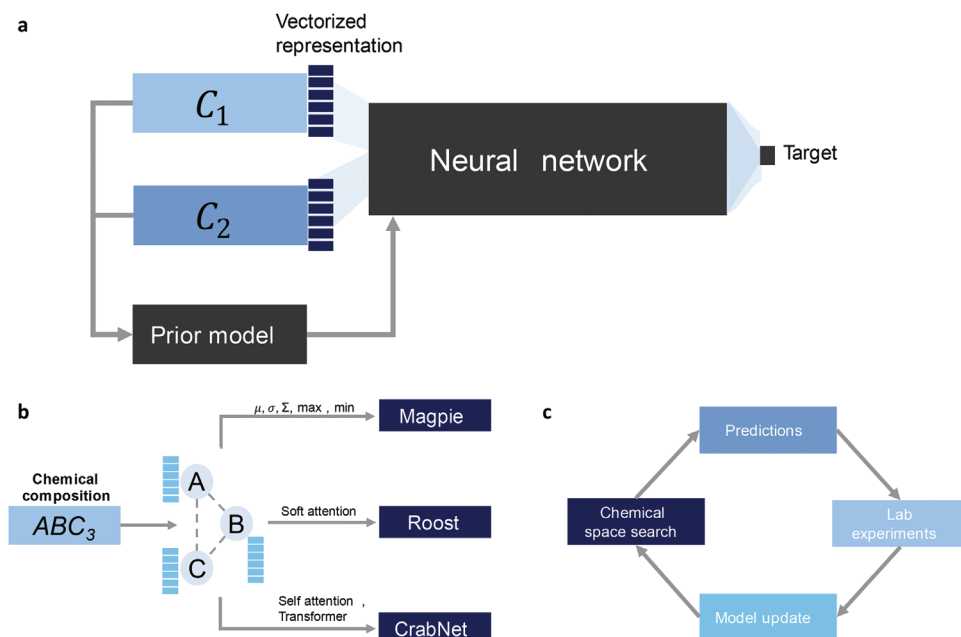
Figure 1. Error correction learning to enable closed-loop materials discovery. a) The approach taken herein to performing error-correction learning (ECL) on predictions from a pre-trained machine learning model, addressed as the Prior model. The error-correction network takes two chemical compositions (C_1 and C_2) as inputs and predicts if C_1 has a power factor larger than C_2. b) Three approaches employed and compared for the purpose of vectorial representation of chemical compositions. Magpie[40] generates vectorial representation using basic statistical operations such as summation, average, standard deviation, min, and max operations on elemental properties. Roost[38] uses a soft-attention based mechanism and converts stoichiometric graphs to numerical vectorial representations. CrabNet[37] generates a numerical representation for chemical compositions using self-attention and transformer architecture. We benchmark all these approaches using their accuracy on literature data and accuracy on collected experimental data. c) Our closed-loop approach: we start with the model and make predictions within the chemical space. The top candidates are used for lab experimentation and fed back to our error correction module for improving prediction accuracy.

We hypothesized that a data-driven strategy for information transfer between the available and acquired data could overcome the first limitation. The problem of uniformly sampling the materials space to acquire an informed prior can then be addressed independently: it becomes equivalent to the development of accurate ML surrogate models. We combine these two strategies, and demonstrate a two-step error correction learning approach: learning from existing datasets and iterative refinements with new experimental results (**Figure 1** for details of the discovery process).

We apply this strategy to the discovery of earth-abundant and low-temperature thermoelectric materials (300 K) via optimization of the experimental power factors (PF). We explore the material space through the synthesis of new inorganic compounds, finding that doping and alloying lead to the family of low-temperature thermoelectric materials PbSe:SnSb. The predicted best candidate exhibits a power factor 2× that of PbSe, and is the highest among previously reported low-temperature-(<300 °C)-synthesized materials. In the process, we find that chemical representation as well as the accuracy of ML models on available datasets play quantitatively significant roles in accelerating closed-loop materials discovery. Exploration using DFT of the origins of higher power factor shows the interaction of Se and Sb in PbSe:SnSb leads to a reduced hole effective mass and increased power factors. The work shows that ECL-based closed-loop approaches account for factors traditionally difficult to parameterize in materials discovery.

2. Results and Discussion

2.1. Error-Correction Learning with Experiments

In a standard ML-based materials screening pipeline, one learns the mapping between material structures/compositions and the outcome variable(s) of interest.[35–38] The trained model is used to screen large chemical spaces and rank the promising candidates. The top-ranked candidates are then validated experimentally.[8,39] However, synthesis conditions such as the synthesis method (hydrothermal or sputtering or ball milling), morphologies (powder or single crystal or nanoparticles), postsynthesis treatment (annealing or etching), state of the precursors (metal salts or metal alkoxides), and source of energy (microwave or ultrasound or laser) differ from one experimental laboratory to another. These potentially significant factors are difficult to parameterize, making it hard to predict synthetic outcomes using ML models trained on historical data, especially from lab to lab. As a result, additional experiments within a new lab are required to explore the chemical space and find the optimal material candidate.

With this in mind, we formulate the challenge as an error-correction problem: the observed outcomes of our in-lab experiments (denoted by y) for two compositions c_1 and c_2 can be expressed as

$$y = \begin{cases} 0 \text{ if } \mathrm{PF}\left(c_1, T_1\right) \geq \mathrm{PF}\left(c_2, T_2\right) \\ 1 \text{ if } \mathrm{PF}\left(c_1, T_1\right) < \mathrm{PF}\left(c_2, T_2\right) \end{cases} \quad (1)$$

**ADVANCED
SCIENCE NEWS**

www.advancedsciencenews.com

**ADVANCED
MATERIALS**

www.advmat.de

where c_1 and c_2 are the materials we wish to compare, T_1 and T_2 are the temperatures at which we make the comparison, and PF(·) represents the in-lab measured power factor (or generally any other property of interest). γ is dependent on the synthesis parameters and methods. It is thus not easy to merge γ with existing datasets coherently and train the ML model on the combined data. Instead, we propose to model the observed outcome γ using an error-correction strategy

$$\gamma \approx g_\theta\left(X_1, X_2, T_1, T_2, m\right) \tag{2}$$

where X_1 and X_2 are vectorial representations for the two materials compositions c_1 and c_2 to be compared; T_1 and T_2 are the temperatures at which to make the comparison; PF(·) represents the power factor (or other property of interest) and m is the prior model trained on existing datasets as one would do in a high-throughput ML search pipeline. The exact form of the error correction function is unknown. To avoid parametric biases, we use a dense neural network, g_θ that can learn from data to model the error correction function (Figure 1a). The proportion of error correction that is achievable depends on the quantity of data, model m, and methods used for the vectorial representation of chemical compositions.

We hypothesize that error-correction learning (ECL) enables correction of the predictions made by the ML model trained on a historical dataset. The neural network g_θ learns to map the experimental quantities obtained under a certain set of consistent experimental conditions to the new set of experimental conditions. By choosing a neural network (or generic machine learning model with good accuracy), we learn implicitly to account for the factors that have led to changes in experimental observations between historical data and our experiments.

2.2. Discovery of Large Power Factor Thermoelectrics

We apply error-correction learning to the discovery of promising thermoelectric materials. We pursue it by first training a prior model on existing data. For training we use a dataset of thermoelectric materials and their experimental properties[41] compiled in a recent study.[8] The dataset reports thermoelectric metrics: conductivity (σ), figure-of-merit (zT), and power factor (PF), measured experimentally in the lab for 573 doped and alloyed materials, spanning 52 distinct elements. These elements are highlighted in the periodic table of Figure S1 in the Supporting Information. The distribution of the material compositions and reported power factors within this dataset are visualized in Figure S2 in the Supporting Information. The dataset covers a diverse set of chemical compounds comprising oxides, other chalcogenides, silicides, germanides, metal alloys, and antimonides.

We train ML regression models to predict the PFs using material compositions and measurement temperatures as predictors. We use the TPOT library to perform model search, optimal preprocessing step selection and hyperparameter tuning.[42] TPOT searches through various ML models (support vector machines, linear regressions, gradient boosted trees, random forests, decision trees, gaussian processes) and their combinations to find the model with the best performance. For training, the entire dataset is randomly split between 80% training

and 20% testing dataset. Hyperparameter optimizations are performed using fivefold cross-validation seeking to maximize the cross-validation coefficient of determination (r^2) between target and predicted values. Furthermore, since material compositions can be represented using various methods, we test three distinct representations—Magpie,[40] Roost,[38] and CrabNet[37] and choose the one with the best cross-validation score as the prior model for driving closed-loop experiments. Figure 1b shows a high-level summary of how these three representations differ. We use transfer learning for training with Roost and CrabNet approaches due to the relatively smaller size of the dataset. The features extracted after the global pooling layer are used to represent different compositions and as input features to train the model (refer to Notes S1 and S2 in the Supporting Information for details on ML model training and the models considered).

Interestingly, the prior model trained using Magpie showed the best cross-validation performance outperforming Roost and CrabNet (refer to **Figure 2**a for a comparison of various representations and ML models we trained and compared). We explore this observation by analyzing the distribution of the generated representations by each of the methods (Figure S3, Supporting Information). Due to its min-max operators, we observe that Magpie generates a less smooth representation that can better capture the doping and alloying effects. On the other hand, Roost and CrabNet have smoother changes in the representation vectors for different materials and that is reflected through lower accuracies for power factor prediction, a property sensitive to small amounts of alloying and doping. Furthermore, to establish the efficacy of TPOT in finding the optimal ML models, we also separately train and optimize the hyperparameters of the Random Forest regression model using the same training-testing splits and same number of cross-validation splits (Figure 2a; Notes S1 and S2, Supporting Information).

After training the prior model, we explore the chemical space to discover low-temperature large power factor materials. In exploration, we limit ourselves to specific precursors and elements. We focused on materials synthesized below <300 °C and avoided regulated materials from the list {As, Cd, Hg, Te, Tl}. Chalcogenides present as part of the material precursors are further screened based on their power factors (PFs) reported in the Materials Project.[43] This results in the list of available precursors (Note S3 in the Supporting Information for the complete list).

As the first step, we measure the experimental PF for all the chalcogenide compositions in their original phase (i.e., without any alloying or doping). The error-correcting dense neural network (DNN) is then trained using the MagPie representation and predictions of prior model as inputs. The model is trained to predict the binary comparison variable using the experimentally measured in-lab power factor (refer to Equation (1) for the definition of this binary variable). We optimize the hyperparameters and estimate the generalization using fivefold cross-validation accuracy. The most generalizable model is then used to explore a new set of compositions for peak performance at 300 K that is fed back, and the cycle is repeated. We explored different material engineering strategies in every round: composites, alloys and dopants (Note S4 in the Supporting Information for more details). We also list each of the compounds tested within every round of experimentation in Note S4 in the Supporting Information. With every round of experimentation, the ability of the

**ADVANCED
SCIENCE NEWS**

www.advancedsciencenews.com

**ADVANCED
MATERIALS**

www.advmat.de
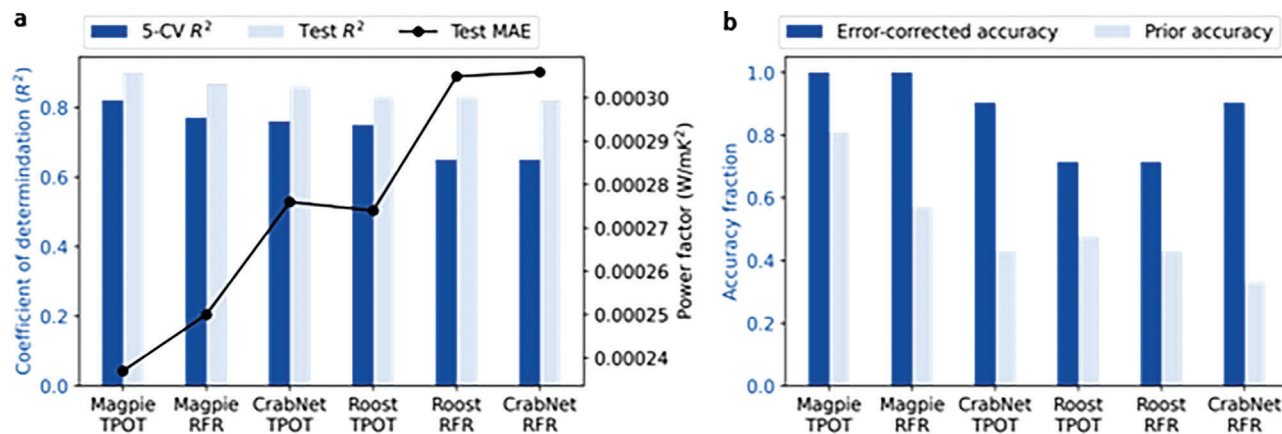
Figure 2. Performance of machine learning models with and without ECL on available and acquired data. a) Performance of the model with the best set of hyperparameters chosen based on the cross-validation performance quantified using mean absolute error (MAE) and coefficient of determination (R^2). We found that Magpie[40] based featurization outperformed transfer learning using Roost[38] and CrabNet.[37] Here, the suffixes TPOT and RFR refer to the model used to belong to the one found by the TPOT library and Random Forest Regressor respectively. The ML model found by the TPOT library for all 3 representations is a combination of multiple ML models. Refer to Note S2 in the Supporting Information for the exact architecture and hyperparameters. b) Performance for each model before and after performing ECL as described in the study. The prior accuracy is measured across all compositions and temperatures based on power factor ranking. The error-corrected accuracy is reported based on ordering at 219 $^{\circ}$C. ECL improves the accuracy for all cases. The improvement, however, depends upon both on featurization used and the initial prior model. The improvement varies as much as 0.16–0.40.

error-correction model to account for the experimental changes improves (Figure 1c for the schematic on workflow). Multiple rounds of the feedback loop and exploration finally yield (PbSe):(2 wt% SnSb) as the optimal composition (refer to the section below for details on experimental characterization). We terminate the feedback loop if the top predicted material candidate remains unchanged after retraining the error-correction model using all the experimental data, including the latest round of experiments.

The results of hyperparameter optimizations are summarized in Figure S4 in the Supporting Information. To establish a baseline, we also evaluate random forest classifiers and gradient boosting classifiers for their error-correction capacity using cross-validation accuracy (Note S5, Supporting Information) and find that they underperform as compared to DNNs.

We compare the effect of change in the prior model on the accuracy of the error-correction learning (ECL) model (Figure 2b). For this, we train the error correction model on all the data collected from the experiments conducted before the last round of experiments. The accuracy is then evaluated on the last unseen round of experiments. We find that higher accuracy prior models lead to higher accuracy on error-corrected predictions. Interestingly, models sharing the same chemical representation also tend to perform similarly, i.e., Magpie-based models, even though differing in prior model's accuracy show high error-corrected accuracies. Similarly, both the CrabNet-based models show similar accuracies post error correction. This observation aligns with the discussion before on the origin of higher accuracy observed with Magpie-based representation (Figure S3, Supporting Information). This indicates that choosing an appropriate representation is essential while driving closed-loop experimentation. We also compared these results to the case where we used a weight-sharing network instead of a DNN. The trends were similar but with lower accuracy (Figure S5, Supporting Information).

The effectiveness of error-correction learning depends upon the specific chemical representation utilized, a finding that highlights the sensitivity of the approach to the choice of representation. It therefore becomes important for practitioners to choose the appropriate chemical representation. The choice, as demonstrated in this study, can be made based on cross-validation accuracy once the first round of experiments has been performed. This choice can also be seen in the form of a trade-off between computation power and number of experiments. Validating and testing different representations to find better error-correcting models require more computation time (for instance a few GPU hours if training neural networks). This increase in computation cost allows us to reduce the number of experiments that need to be performed.

We find that the next-best model CrabNet, after error correction on the ranking of compounds, underperforms. As a result, at least one more round of experimentation is needed to reach the optimal candidate (Figure 2b). Thus, the accurate prior model developed herein reduces the number of experiments by at least (1/5 × 100%) = 20% (the total number of rounds of experiments in such a scenario would be 5). The best candidate composition $(PbSe)_{0.98}(SnSb)_{0.02}$ is ranked at 98th if the material candidates are ranked according to the order of decreasing power factors using the most accurate prior model. Thus, compared to the conventional high-throughput screening approach of testing the high-ranked predictions from the prior model, the current approach reduces the number of candidates that need to be tested by as much as 83%, i.e., less than 1/3rd the number of experiments that would need to be conducted. We also compare our approach to a modified version of the previously proposed data fusion approach[28] in **Table 1** (refer to Note S6 in the Supporting Information for implementation details).

**ADVANCED
SCIENCE NEWS**

www.advancedsciencenews.com

**ADVANCED
MATERIALS**

www.advmat.de
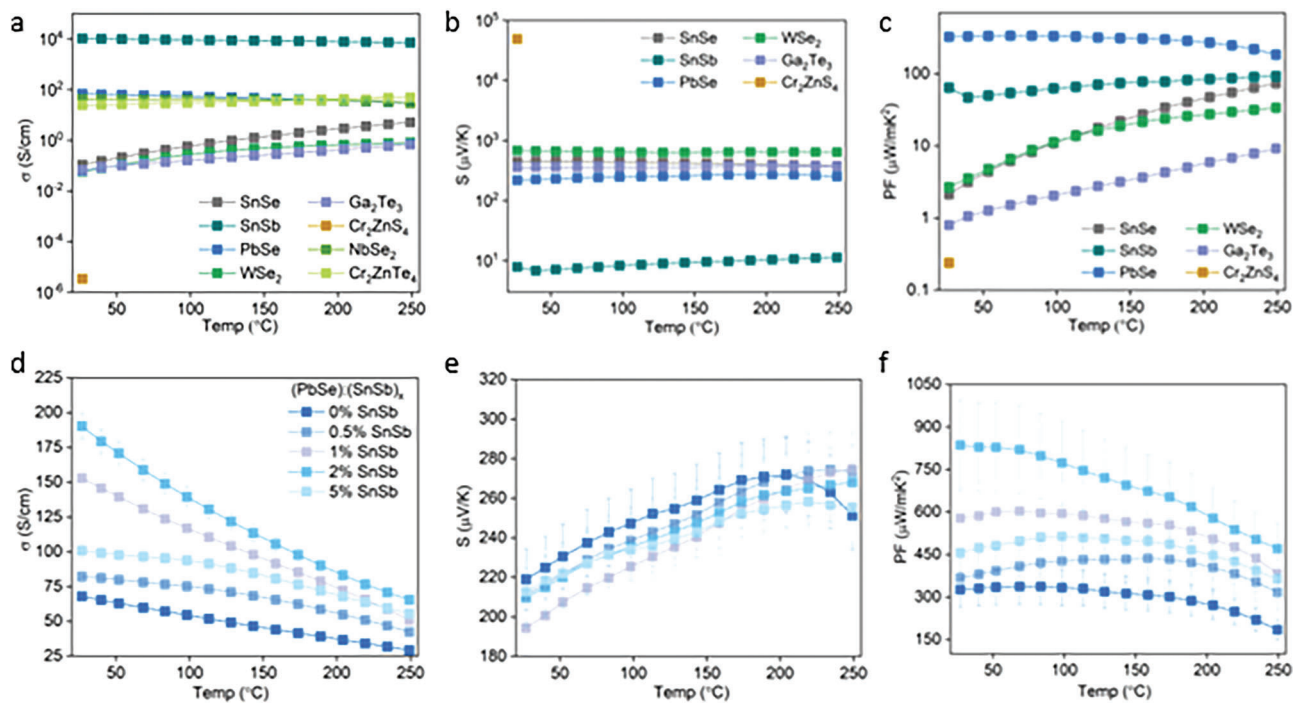
Figure 3. Thermoelectric performance of materials measured experimentally. a–c) Show conductivity (σ), Seebeck coefficient (S), and power factor (PF) trends for stoichiometric compounds as a function of temperature. PbSe shows the highest power factor due to a balance between conductivity and Seebeck coefficient. d–f) σ, S, and PF trends for our predicted most promising compositions $(PbSe):(SnSb)_x$. We observe that the best composition has a power factor twice that of the undoped PbSe.

Table 1. We tabulate the accuracy and compare a former approach that requires defining rules for data fusion to our approach that utilizes dense neural networks for error correction.

| Method	Accuracy on the final-round data at 219 °C
Probabilistic constraint data-fusion[28]	0.57
ECL (this study)	0.99

2.3. Experimental Validation

While the synthesis of inorganic compounds by solution method is tedious due to the limited number of suitable metal salts and solubility issues, vacuum techniques require an extensive amount of time for optimization. As such, we adopted ball milling to synthesize some of the predicted compounds owing to its high yield and faster optimization rate. We tested the top candidates from ML predictions and evaluated the compounds' thermoelectric properties. The measured properties were fed to the error correction module to improve the accuracy.

We observe that the highest electrical conductivity (σ) was obtained for SnSb with a low Seebeck coefficient (S). Stoichiometry change and forming composite with PbI_2 did not improve Seebeck of SnSb. However, its combination with PbSe resulted in balanced σ and S. Temperature-dependent σ and S (refer to the characterization subsection of the Experimental Section for more details) of the stoichiometric compounds, SnSe, Wse_2, GaTe, and $CrZnTe_4$ exhibit semiconducting behavior while SnSb,

PbSe, and $NbSe_2$ show metallic behavior. Notably, $CrZnS_4$ has extremely low electrical conductivity and consequently high Seebeck (**Figure 3**a–c). The highest electrical conductivity is observed in the case of SnSb (>10 000 S cm^{-1}) which leads to a very low Seebeck coefficient. PbSe exhibits the largest power factor among the stoichiometric compounds due to balanced electrical conductivity and Seebeck. Despite of extraordinary conductivity of SnSb, its modest power factor is a consequence of low Seebeck. In contrast, PbSe shows good Seebeck, but its electrical conductivity is not very high (We compare conductivities of many composites made and tested but not added to Figure 3b in Figure S6 in the Supporting Information).

These findings align with the prediction that addition of SnSb to PbSe improves the power factor. We observe that small amounts of SnSb addition enhance the electrical conductivity of PbSe with a minor decrease in Seebeck (refer to materials subsection of the Experimental Section for details on synthesis and materials). Therefore, the PbSe/SnSb composition results in a high power factor of more than 850 μW mK^{-2} at room temperature for 2 wt% SnSb, and good performance is observed in the whole temperature regime (Figure 3d–f). Such a high-power factor for the present composite is comparable to state-of-the-art polycrystalline thermoelectric materials prepared by similar methods (Figure S7, Supporting Information). High performance room-temperature thermoelectric materials are particularly lucrative for various applications including sensors, heat spreaders, internet of things and portable electronics.[44] We would like to point out that most high-performance thermoelectric materials are synthesized by high-temperature techniques in the form of

ADVANCED
SCIENCE NEWS

www.advancedsciencenews.com

ADVANCED
MATERIALS

www.advmat.de
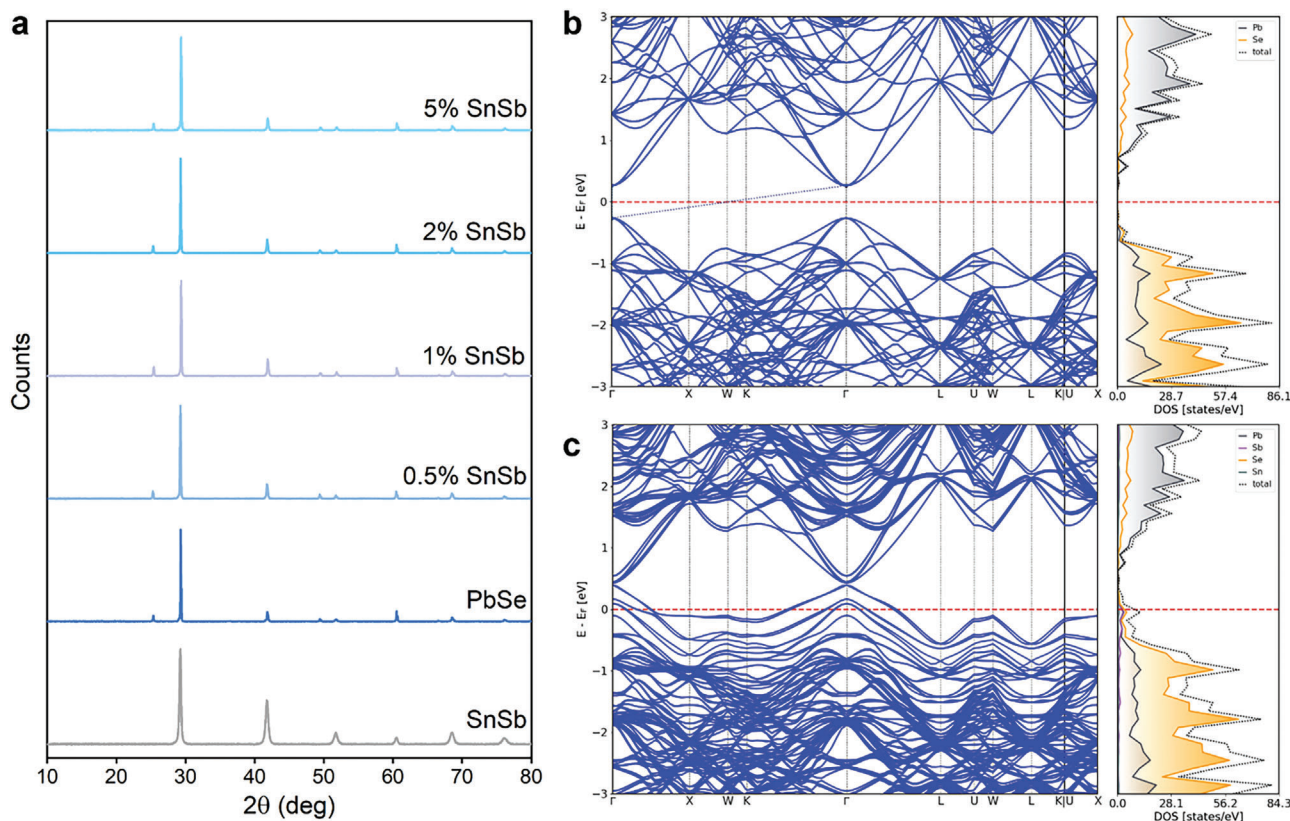
Figure 4. Structural and DFT analysis of the best thermoelectric candidates a) shows XRD plots for (PbSe):(SnSb)$_x$ composite. b) Band structure of PbSe along the high-symmetry path. c) shows band structure of (PbSe):(2 wt% SnSb) along the high-symmetry path in the reciprocal space. The change in curvature of the state just below the defect state in the valence band leads to a reduction in the effective mass and therefore, improved transport properties (refer to Figures S10 and S11 in the Supporting Information for close-ups).

single crystals whereas in the present work, polycrystalline materials are used without any extensive processing giving comparable performances at 300 K. It should be noted that further performance improvement can be anticipated by additional processing techniques, such as spark plasma sintering, generally employed in the case of high-performance thermoelectric materials.

2.4. Origins of High Power Factor

To increase understanding of the atomistic origin of the high performance of (PbSe)$_{0.98}$(SnSb)$_{0.02}$, we perform density functional theory (DFT) calculations (refer to the DFT subsection of the Experimental Section for details). We obtain the unit cell for the PbSe supercell from Materials Project[43] and use it to construct a 216 atoms supercell. Experimental X-ray diffraction (XRD) indicates that a small amount of alloying does not change the structure (**Figure 4**a). We use this information to optimize the geometry of the SnSb doped PbSe supercell by relaxing only the atomic positions and keeping the lattice constants fixed using the generalized gradient approximation (GGA) exchange-correlation (xc) functional (refer to Figures S6 and S7 for pictorial representation). We perform self-consistent HSE06 xc-functional calculations on the pristine and doped relaxed structures while incorporating spin–orbit coupling (SOC). Comparing the electronic

structure of PbSe with PbSe:SnSb, we observe that the introduction of Sn and Sb modulates the density of states (DOS) near conduction band minimum (CBM) and valence band maximum (VBM) respectively. This modulation decreases the hole effective mass, improving the overall transport property of the PbSe:SnSb composite (Figure 4b,c) thereby resulting in a larger power factor. Please refer to Figures S10 and S11 (Supporting Information) for effective mass fitting plots.

3. Conclusions

We have developed and demonstrated a two-step error correction learning approach to performing theory-driven closed-loop experimental exploration of thermoelectric materials. In the process, we trained an ML model that outperformed prior models in the accurate prediction of experimental power factors. This improvement in accuracy reduces the number of in-lab experiments. The approach enables discovery of a thermoelectric material (PbSe)$_{0.98}$:(SnSb)$_{0.02}$ that exhibits a large power factor. DFT simulations show that the performance improvements are mainly a result of the chemical interactions and not structure distortions. The approach to thermoelectric materials may well be extended to the discovery of materials for applications requiring high conductivity and improved optoelectronic properties.

4. Experimental Section

Data: The dataset collected by DopNet[8] authors from the Materials Research Laboratory (MRL) are used for training the prior models. It is available at https://github.com/ngs00/DopNet and the original data can be found at http://www.mrl.ucsb.edu:8080/datamine/thermoelectric.jsp. Data based on in-lab experiments is available at https://github.com/hitarth64/TherML.

Code Availability: All the code and data used for this study are available as open source at https://github.com/hitarth64/TherML. All the trained models were also provided so that they can be used for future explorations.

Materials: Sn, Se, S, Zn, Te, and Cr powders were purchased from Sigma-Aldrich. PbSe, Sb, and WSe_2 were purchased from Alfa-Aesar. $NbSe_2$, GaSe, and Ga_2Te_3 were procured from American Elements.

SnSe, SnSb, Cr_2ZnS_4, and Cr_2ZnTe_4 were synthesized by ball milling stoichiometric amounts of precursors for 8, 15, 32, and 32 h at 30 Hz, respectively. All composites were obtained by ball milling the respective compounds (e.g., SnSe and SnSb) for 20 min at 30 Hz.

Characterization: Electrical conductivity and Seebeck measurements were performed on Netzsch SBA 548 Nemesis thermoelectric set up under He environment. Samples were prepared by loading the powders into a steel compaction die and compressing them to form pellets for thermoelectric measurements. All pellets were annealed at 250 °C inside an N_2 glovebox before thermoelectric measurements. The instrument uncertainty for electrical conductivity and Seebeck measurements are ±5% and ±7%, respectively. As a result of the very low electrical conductivity of Cr_2ZnS_4, room temperature Seebeck was measured using a manual setup consisting of Peltier devices and a thermocouple. For thermal voltage measurements, a homemade setup was used with Peltier devices and thermocouples to apply the temperature gradient across the sample, and the voltage was recorded using a Keithley 6517B electrometer. XRD was measured using Bruker D8 Advance.

Density Functional Theory: All DFT relaxations are performed using Vienna Ab initio Simulation Package (VASP) 6.2.1. We used the Perdew–Burke–Ernzerhof (PBE)[45] exchange-correlation functional for geometry optimization of the material systems. The energy cut-off for the plane wave was set to 520 eV. The energy threshold for self-consistent energy convergence was set to 10^{-3} eV whereas the global convergence threshold was set to 10^{-2} eV energy difference between two successive ionic steps. A smearing width of 0.05 eV, consistent with the Materials Project, was chosen for calculations. Calculations were performed over a uniform k-points grid of $2 \times 2 \times 2$ generated using the Monkhorst scheme.[46]

Given the optimized geometry, static DFT calculation was performed using hybrid HSE06[47] functional while incorporating the spin–orbit coupling (SOC) effect over high-symmetry points of the reciprocal lattice using all-electron DFT code FHI-AIMS.

Supporting Information

Supporting Information is available from the Wiley Online Library or from the author.

Acknowledgements

Conflict of Interest

The authors declare no conflict of interest.

Data Availability Statement

The data that support the findings of this study are openly available in TherML at https://github.com/hitarth64/TherML.

Keywords

[1] P. Jood, M. Ohta, A. Yamamoto, M. G. Kanatzidis, *Joule* **2018**, *2*, 1339.
[2] G. Tan, M. Ohta, M. G. Kanatzidis, *Philos. Trans. R. Soc. A* **2019**, *377*, 20180450.
[3] S. Vostrikov, A. Somov, P. Gotovtsev, *Appl. Energy* **2019**, *255*, 113786.
[4] N. Van Toan, T. Thi Kim Tuoi, N. Van Hieu, T. Ono, *Energy Convers. Manage.* **2021**, *245*, 114571.
[5] D. W. Davies, K. T. Butler, A. J. Jackson, A. Morris, J. M. Frost, J. M. Skelton, A. Walsh, *Chem* **2016**, *1*, 617.
[6] H. Choubisa, M. Askerka, K. Ryczko, O. Voznyy, K. Mills, I. Tamblyn, E. H. Sargent, *Matter* **2020**, *3*, 433.
[7] H. Choubisa, J. Abed, D. Mendoza, H. Matsumura, M. Sugimura, Z. Yao, Z. Wang, B. R. Sutherland, A. Aspuru-Guzik, E. H. Sargent, *Matter* **2023**, *5*, 605.
[8] G. S. Na, S. Jang, H. Chang, *npj Comput. Mater.* **2021**, *7*, 106.
[9] S. Chakraborty, W. Xie, N. Mathews, M. Sherburne, R. Ahuja, M. Asta, S. G. Mhaisalkar, *ACS Energy Lett.* **2017**, *2*, 837.
[10] G. Ding, G. Gao, K. Yao, *Sci. Rep.* **2015**, *5*, 9567.
[11] A. Jain, Y. Shin, K. A. Persson, *Nat. Rev. Mater.* **2016**, *1*, 15004.
[12] H. Zhu, G. Hautier, U. Aydemir, Z. M. Gibbs, G. Li, S. Bajaj, J.-H. Pöhls, D. Broberg, W. Chen, A. Jain, M. A. White, M. Asta, G. J. Snyder, K. Persson, G. Ceder, *J. Mater. Chem. C Mater.* **2015**, *3*, 10554.
[13] J. M. Hodges, Y. Xia, C. D. Malliakas, G. C. B. Alexander, M. K. Y. Chan, M. G. Kanatzidis, *Chem. Mater.* **2018**, *30*, 7245.
[14] Vikram, B. Sahni, A. Jain, A. Alam, *ACS Appl. Energy Mater.* **2022**, *5*, 9141.
[15] C. Barreteau, J.-C. Crivello, J.-M. Joubert, E. Alleno, *Comput. Mater. Sci.* **2019**, *156*, 96.
[16] A. Jain, A. J. H. Mcgaughey, *Phys. Rev. B* **2016**, *93*, 081206.
[17] N. Andrejevic, J. Andrejevic, B. A Bernevig, N. Regnault, F. Han, G. Fabbris, T. Nguyen, N. C. Drucker, C. H. Rycroft, M. Li, *Adv. Mater.* **2022**, *34*, 2204113.
[18] V. Tshitoyan, J. Dagdelen, L. Weston, A. Dunn, Z. Rong, O. Kononova, K. A. Persson, G. Ceder, A. Jain, *Nature* **2019**, *571*, 95.
[19] K. Pal, C. W. Park, Y. Xia, J. Shen, C. Wolverton, *npj Comput. Mater.* **2022**, *8*, 48.
[20] Z. Ren, S. I. P. Tian, J. Noh, F. Oviedo, G. Xing, J. Li, Q. Liang, R. Zhu, A. G. Aberle, S. Sun, X. Wang, Y. Liu, Q. Li, S. Jayavelu, K. Hippalgaonkar, T. Jung, T. Buonassisi, *Matter* **2022**, *5*, 314.
[21] N. Wang, B. Yuan, C. Tang, L. Du, R. Zhu, Y. Aoki, W. Wang, L. Xing, S. Ye, *Adv. Mater.* **2022**, *34*, 2203446.
[22] J.-H. Pöhls, S. Chanakian, J. Park, A. M. Ganose, A. Dunn, N. Friesen, A. Bhattacharya, B. Hogan, S. Bux, A. Jain, A. Mar, A. Zevalkink, *Mater. Horiz.* **2021**, *8*, 209.
[23] M. Miyata, T. Ozaki, T. Takeuchi, S. Nishino, M. Inukai, M. Koyano, *J. Electron. Mater.* **2018**, *47*, 3254.

**ADVANCED
SCIENCE NEWS**

www.advancedsciencenews.com

**ADVANCED
MATERIALS**

www.advmat.de

[24] T. Jia, Z. Feng, S. Guo, X. Zhang, Y. Zhang, *ACS Appl. Mater. Interfaces* **2020**, *12*, 11852.

[25] K. Choudhary, K. F. Garrity, F. Tavazza, *J. Phys.: Condens. Matter* **2020**, *32*, 475501.

[26] Z. Hu, W. Wu, Q. Wang, X. Shao, *J. Phys. Chem. C* **2022**, *126*, 12735.

[27] Z. Hou, Y. Takagiwa, Y. Shinohara, Y. Xu, K. Tsuda, *ACS Appl. Mater. Interfaces* **2019**, *11*, 11545.

[28] S. Sun, A. Tiihonen, F. Oviedo, Z. Liu, J. Thapa, Y. Zhao, N T. P. Hartono, A. Goyal, T. Heumueller, C. Batali, A. Encinas, J. J. Yoo, R. Li, Z. Ren, I. M Peters, C. J. Brabec, M. G. Bawendi, V. Stevanovic, J. Fisher, T. Buonassisi, *Matter* **2021**, *4*, 1305.

[29] J. Wagner, C. G. Berger, X. Du, T. Stubhan, J. A. Hauch, C. J. Brabec, *J. Mater. Sci.* **2021**, *56*, 16422.

[30] B. P. Macleod, F. G. L. Parlane, T. D. Morrissey, F. Häse, L. M. Roch, K. E. Dettelbach, R. Moreira, L. P. E. Yunker, M. B. Rooney, J. R. Deeth, V. Lai, G. J. Ng, H. Situ, R. H. Zhang, M. S. Elliott, T. H. Haley, D. J. Dvorak, A. Aspuru-Guzik, J. E. Hein, C. P. Berlinguette, *Sci. Adv.* **2020**, *6*, eaaz8867.

[31] B. Burger, P. M. Maffettone, V. V. Gusev, C. M. Aitchison, Y. Bai, X. Wang, X. Li, B. M. Alston, B. Li, R. Clowes, N. Rankin, B. Harris, R. S. Sprick, A. I. Cooper, *Nature* **2020**, *583*, 237.

[32] A. G Kusne, H. Yu, C. Wu, H. Zhang, J. Hattrick-Simpers, B. Decost, S. Sarker, C. Oses, C. Toher, S. Curtarolo, A. V. Davydov, R. Agarwal, L. A. Bendersky, M. Li, A. Mehta, I. Takeuchi, *Nat. Commun.* **2020**, *11*, 5966.

[33] M. Wu, E. Tikhonov, A. Tudi, I. Kruglov, X. Hou, C. Xie, S. Pan, Z. Yang, *Adv. Mater.* **2023**, *35*, 2300848.

[34] C. Lampe, I. Kouroudis, M. Harth, S. Martin, A. Gagliardi, A. S. Urban, *Adv. Mater.* **2023**, *35*, 2208772.

[35] C. W. Park, C. Wolverton, *Phys. Rev. Mater.* **2019**, *4*, 063801.

[36] T. Xie, J. C. Grossman, *Phys. Rev. Lett.* **2018**, *120*, 145301.

[37] A .Y.-T. Wang, S. K. Kauwe, R. J. Murdock, T. D. Sparks, *npj Comput. Mater.* **2021**, *7*, 77.

[38] R. E. A. Goodall, A. A. Lee, *Nat. Commun.* **2020**, *11*, 6280.

[39] M. Askerka, Z. Li, M. Lempen, Y. Liu, A. Johnston, M. I. Saidaminov, Z. Zajacz, E. H. Sargent, *J. Am. Chem. Soc.* **2019**, *141*, 3682.

[40] L. Ward, A. Agrawal, A. Choudhary, C. Wolverton, *npj Comput. Mater.* **2016**, *2*, 16028.

[41] M. W. Gaultois, T. D. Sparks, C. K. H. Borg, R. Seshadri, W. D. Bonificio, D. R. Clarke, *Chem. Mater.* **2013**, *25*, 2911.

[42] T. T. Le, W. Fu, J. H. Moore, *Bioinformatics* **2020**, *36*, 250.

[43] A. Jain, S. P. Ong, G. Hautier, W. Chen, W. D. Richards, S. Dacek, S. Cholia, D. Gunter, D. Skinner, G. Ceder, K. A. Persson, *APL Mater.* **2013**, *1*, 011002.

[44] J. Chen, H. Yuan, Y.-K. Zhu, K. Zheng, Z.-H. Ge, J. Tang, D. Zhou, L. Yang, Z.-G. Chen, *Inorg. Chem.* **2021**, *60*, 14165.

[45] J. P. Perdew, K. Burke, M. Ernzerhof, *Phys. Rev. Lett.* **1996**, *77*, 3865.

[46] H. J. Monkhorst, J. D. Pack, *Phys. Rev. B* **1976**, *13*, 5188.

[47] J. Heyd, G. E. Scuseria, *J. Chem. Phys.* **2004**, *121*, 1187.